Optics Communications 493 (2021) 126999

Contents lists available at ScienceDirect

Optics Communications

journal homepage: www.elsevier.com/locate/optcom

A new route to designing a one-dimensional multiperiodic photonic crystal with adjustable photonic band gap and enhanced electric field localization

Farideh Sadat Saeidi, Mehrdad Moradi *

Institute of Nanoscience and Nanotechnology, University of Kashan, Kashan 87317, Iran

ARTICLE INFO

Keywords:
1-D photonic crystal
Adjustable band gap
Electric field localization
Defect

ABSTRACT

In this paper, photonic band gap (PBG) properties and electric field distribution of a one-dimensional multiperiodic photonic crystal were theoretically calculated based on a 2 × 2 transfer matrix method (TMM) using MATLAB software. Stacked layers of Nb_2O_5, Si and TiO_2 were designed as a new model of the one-dimensional three-periodic photonic crystal. The results show that by changing parameters such as the layers order, number of periods, thickness of layers, defect layer thickness and the angle of incident, it is possible to engineer the width and position of PBG while also increasing the electric field intensity inside the photonic crystal. It is shown, that the $[NS]^2$ $[T]^1$ $[NS]^8$ structure (N = Nb_2O_5, S = Si and T = TiO_2) has a wider photonic band gap (PBG) allowing for applications such as laser eye protections. The $[NS]^2$ $[T]^2$ $[NS]^8$ structure is found to be the highest in terms of localization of light in defect layer and being suitable for use in the photocatalysis field.

1. Introduction

During the last decades, a great deal of attention has been devoted to photonic crystals (PCs) as a new type of materials [1–4], whose optical properties are used to manipulate the light on the scale of the wavelength. Photonic crystals materials, also known as photonic microstructures or photonic bandgap (PBG) structures, are periodic optical structures in one, two, and three dimensions (1D, 2D, and 3D) with a lattice constant comparable to the wavelengths of electromagnetic waves (EMWs) propagating through the structure [5–10]. In analogy to the forbidden energy (the band gap) for electrons in semiconductors, such materials can show a forbidden spectrum of photons where the light cannot propagate through the crystal. Causing the unique property, many one-dimensional photonic crystal (1D-PC) [11–16] was explored such as reflector [17], omnidirectional reflector [18], multiplexer [19], switches [20], resonator [21], polarization controller [22], filter [23,24], structural colors [25] etc. For example, this type of filter can be used to fabricate laser eye protection glasses [26]. In the eye, visible and near infrared radiation passes through the cornea, and is focused on and absorbed by the retina, it is known as the "retinal hazard region". Also, Ultraviolet radiation may cause negative effects such as increased pigmentation, skin burns, skin aging and skin cancer [27].

TiO_2 in different types and forms has shown great advantages as ideal and powerful photocatalysts [28–30] on account of its chemical stability, nontoxicity, high reactivity and low cost. Photonic crystals (PCs) are also found to be capable of localizing light coherently when the disorder is introduced into the structure, thus making the defect layer break its periodicity, and act as an optical cavity [31–33]. In turn, this allows for a strong interaction between the light and matter. In recent years, TiO_2 has been widely used as a defect layer in PC structures [12]. However, the recombination rate of photogenerated hole–electron pairs on TiO_2 is very high, which greatly reduces the photocatalytic efficiency and limits the industrial application of TiO_2. To control this concern, many different methods have been proposed in the research of TiO_2 photocatalysis, for example, loading some amounts of metal or metal oxide, known as co-catalyst, on the surface of TiO_2 [34,35], or employing TiO_2 with a wide range of materials [36,37], e.g., niobium oxide (Nb_2O_5) [38]. Among oxide semiconductors, Nb_2O_5 is a promising n-type transition metal oxide with numerous significant photocatalytic activities, due to its low extinction coefficient, and high transparent ratio in the UV–vis–NIR (ultraviolet–visible near-infrared) region [39–41]. To the best of our knowledge, Nb_2O_5/TiO_2 layers as promising composite photocatalyst for application in industrial photocatalysis has not been studied well. Many theoretical and numerical tools have been developed to understand EMWs propagation through PC. One of them is transfer matrix method (TMM), a simple, accurate, low-computer-time formalism and low matrix dimensionality [42–46].

The purpose of this work is modification of eye protection glasses and photocatalytic efficiency. To achieve this goal, we propose a new PC to study and ameliorate the transmission spectra of different materials, thicknesses and angles. The second novelty is that we discussed

* Corresponding author.
E-mail address: m.moradi@kashanu.ac.ir (M. Moradi).

https://doi.org/10.1016/j.optcom.2021.126999
Received 24 January 2021; Received in revised form 6 March 2021; Accepted 4 April 2021
Available online 7 April 2021

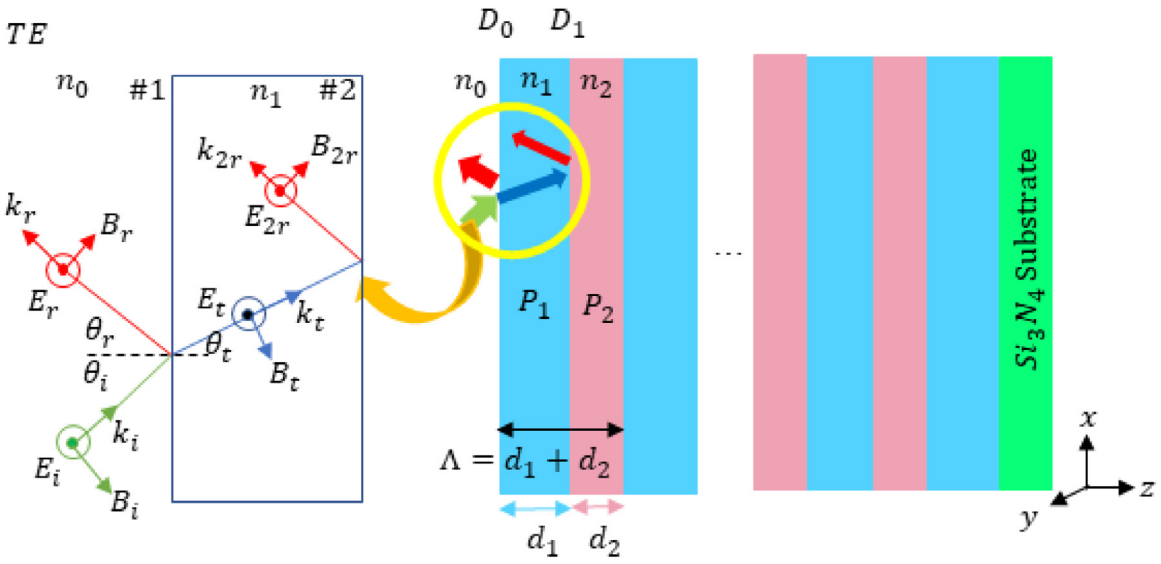

Fig. 1. The schematic representation of reflection and transmission of the TE mode by 1D-PC. The respective wave numbers of the incident, transmitted, and reflected waves are k_i, k_t, and k_{1r} and k_{2r}. The incident, transmitted and reflected angles are denoted as: θ_i, θ_t and θ_r, respectively. The electric field amplitudes are E_i, E_t, E_{1r} and E_{2r}, and the magnetic field amplitudes are B_i, B_t, B_{1r} and B_{2r}. The parameters D and P represent the dynamical and propagation matrices, respectively.

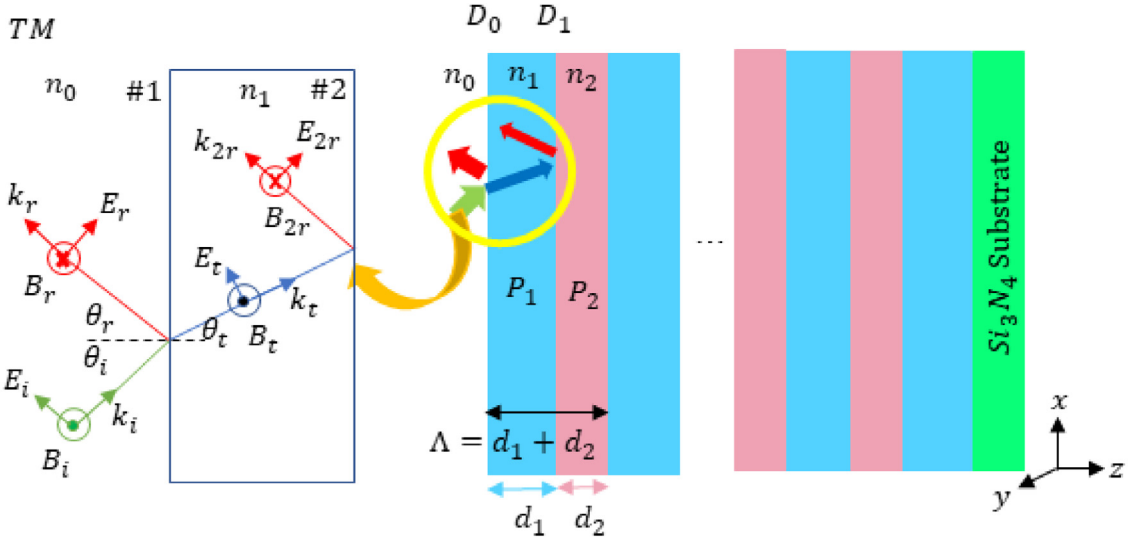

Fig. 2. The schematic representation of reflection and transmission of the TM mode by 1D-PC.

increasing the interaction of light with matter by using the localization of light, so we studied variation of the electric field intensity as a function of the thickness using the method of the transfer matrix.

2. Theory

Using the TMM method, the transmission spectrum and electric field distribution can be considered in 1D-PC. In this respect, the characteristic matrix corresponding to one stack is initially calculated, and then distributed to a PC. Here, a homogeneous and isotropic film with refractive indices n_1 and n_2 is assumed to be deposited on a substrate with the refractive index n_s placed in a medium with n_0, as schematically depicted for transverse electric (TE) and transverse magnetic (TM) modes in Figs. 1 and 2, respectively. As the incident beam (θ_i) hits the air/first layer interface (#1), some of it is reflected from the medium. Meanwhile, the transmitted beam undergoes an internal reflection at the first layer/second layer interface (#2).

When the free charge density or current density at the dielectric boundary is 0, the tangential components of the electric field are continuous across the interface, as expressed in Eq. (1):

$$E_1^{\parallel} - E_2^{\parallel} = 0 \tag{1}$$

Therefore, the electric field can be written as follows:

$$E_i + E_{1r} = E_t + E_{2r} \tag{2}$$

where E_i is the incident amplitude, E_{1r} is the reflected amplitude from the first interface (#1), E_t is the transmitted amplitude, and E_{2r} is the reflected amplitude from the second interface (#2). As the light propagates in the layers, a phase shift [being proportional to the layer thickness and inversely proportional to the wavelength ($\phi = \frac{2\pi}{\lambda} nd\cos\theta$)] occurs due to the geometric path difference between the reflected or transmitted waves. Accordingly, the layer thickness and the wavelength can influence the results. Similarly, according to the boundary conditions of the magnetic field given by Eq. (3), all the tangential magnetic field components are also continuous as expressed in Eq. (4):

$$\frac{B_1^{\parallel}}{\mu_1} - \frac{B_2^{\parallel}}{\mu_2} = 0 \tag{3}$$

$$-B_i\cos\theta_i + B_{1r}cos\theta_i = -B_t cos\theta_t + B_{2r}cos\theta_t \quad (4)$$

where B_i is the incident light wave amplitude, B_{1r} is the reflected light wave amplitude from the interface (#1), B_t is the transmitted light wave amplitude, and B_{2r} is the reflected light wave amplitude from the interface (#2). Next, one can assume $\mu_1 = \mu_2$ and $\theta_i = \theta_r$ (according to the Snell's law). By taking into account $B = \frac{n}{c}E$, the following expression is obtained:

$$n_i E_i \cos\theta_i - n_i E_{1r}\cos\theta_i = n_1 E_{1t}\cos\theta_t - n_1 E_{2r}\cos\theta_t \quad (5)$$

The above-mentioned formulations relate the field components of the first boundary to those of the second one, which can be written in the matrix form as follows:

$$\begin{pmatrix} 1 & 1 \\ n_i cos\theta_i & -n_i cos\theta_i \end{pmatrix}\begin{pmatrix} E_i \\ E_{1r} \end{pmatrix} = \begin{pmatrix} 11 \\ n_1 cos\theta_t - n_1 cos\theta_t \end{pmatrix}\begin{pmatrix} E_t \\ E_{2r} \end{pmatrix} \quad (6)$$

The same calculations are required for the TM mode, as given below:

$$E_i\cos\theta_i + E_{1r}\cos\theta_i = E_t\cos\theta_t + E_{2r}\cos\theta_t \quad (7)$$

$$B_i - B_{1r} = B_t - B_{2r} \quad (8)$$

$$n_i E_i - n_i E_{1r} = n_1 E_{1t} - n_1 E_{2r} \quad (9)$$

$$\begin{pmatrix} cos\theta_i cos\theta_i \\ n_i - n_i \end{pmatrix}\begin{pmatrix} E_i \\ E_{1r} \end{pmatrix} = \begin{pmatrix} cos\theta_t cos\theta_t \\ n_1 - n_1 \end{pmatrix}\begin{pmatrix} E_t \\ E_{2r} \end{pmatrix} \quad (10)$$

Now, a 1D-PC consisting of N periodic arrays of alternating layers is taken into consideration. Here, it is assumed that the layered structure is periodic in the z direction, and homogeneous in the x–y plane. Each stack layer is associated with two kinds of matrices: the dynamical matrix D, and the propagation matrix P. The dynamical matrix (D_j, in which j represents the medium) for TE (s-polarization) and TM (p-polarization) modes is given by Eqs. (11) and (12), respectively:

$$D_j = \begin{bmatrix} 1 & 1 \\ k_j cos\theta_j & -k_j cos\theta_j \end{bmatrix} \quad (11)$$

$$D_j = \begin{bmatrix} cos\theta_j & cos\theta_j \\ k_j & -k_j \end{bmatrix} \quad (12)$$

The translational matrix (P_j, in which j is the layer number) is expressed as follows:

$$P_j = \begin{bmatrix} e^{-ik_j d_j} & 0 \\ 0 & e^{+ik_j d_j} \end{bmatrix} \quad (13)$$

where d_j is the thickness, θ_j is the incident angle, and k_j is the wavenumber ($k_j = \frac{2\pi n_j}{\lambda}$). The transfer matrix of each layer can be represented by:

$$M_j = D_j P_j D_j^{-1} \quad (14)$$

The total transfer matrix of the structure is written as follows:

$$M = \begin{pmatrix} M_{11} & M_{12} \\ M_{21} & M_{22} \end{pmatrix} \quad (15)$$

The transmission and reflection coefficients of the structure are provided with the elements of the transfer matrix as follows:

$$t = \frac{1}{M_{11}}, r = \frac{M_{21}}{M_{11}} \quad (16)$$

Finally, the transmission and reflection can be calculated based on the following relations [16,42–46]:

$$T = \frac{n_s cos\theta_s}{n_0 cos\theta_0}|t|^2 = \frac{n_s cos\theta_s}{n_0 cos\theta_0}\left|\frac{1}{M_{11}}\right|^2, R = |r|^2 = \left|\frac{M_{21}}{M_{11}}\right|^2 \quad (17)$$

where 0 and S denote air and substrate, respectively.

On the other hand, the electric field intensity in a PC can be calculated by estimating the matrix M_F (varying depending on z) inside the structure, as given below:

$$M_F = D_0^{-1}\prod_j D_m P_m D_m^{-1}(D_F P_F D_F^{-1}) \quad (18)$$

These equations allow for deducing the total electric field expression of the TE and TM polarizations as follows [45,46]:

$$\begin{bmatrix} 1 \\ r_{ss} \end{bmatrix} = \overline{M}_F \begin{bmatrix} E_s^+ \\ E_s^- \end{bmatrix}_{z=F} \quad (19)$$

where E^+ is the forward propagating electric field components, and E^- is the backward propagating electric field components of the whole structure:

$$E_s = E_s^+ + E_s^- \quad (20)$$

$$I_s = |E_s|^2 \quad (21)$$

Similarly, the following expressions can be considered for the p-polarization:

$$\begin{bmatrix} 1 \\ r_{pp} \end{bmatrix} = \overline{M}_F \begin{bmatrix} E_p^+ \\ E_p^- \end{bmatrix}_{z=F} \quad (22)$$

$$E_p = E_p^+ + E_p^- \quad (23)$$

$$I_p = |E_p|^2 \quad (24)$$

3. Results and discussion

The propagation of light through a PC is impacted by compositional parameters. Therefore, the transmittance spectrum is modified by manipulating, for instance, refractive indices, layers arrangement, number of periods, thickness of layers, and angle of incident of the constituent materials (Eqs. (11)–(13)). A wide width PBG is formed when the refractive index contrast of the constituent materials is high. Let us consider a 1D-PC structure, which comprises Si for high refractive index layer [47] and Nb_2O_5 as a low refractive index layer, due to its bandgap in visible radiation [39–41]. Also, TiO_2 is chosen to be a defect layer, due to its wide band gap in ultraviolet radiation and photocatalytic behavior [28], and Si_3N_4 as a substrate layer. To fabrication of 1D-PC in such way leads to low processing cost, the starting precursors, from which part that has more layer and if successful, the rest of the layers are made.

1D-PC with two various designs based on the layer arrangement and the number of periods is introduced as {A[NS]$^\alpha$ [T]^1 [NS]$^\beta$ /Sub} and {A[NS]$^\alpha$ [T]^2 [SN]$^\beta$ /Sub}, where A means the air, N is Nb_2O_5, S is Si, T is TiO_2, and Sub denotes Si_3N_4 as substrate. Also, α and β denoting the number of periodicities for the top, and bottom layers of the defects, respectively. Each sub-structure [NS]$^\alpha$ and [SN]$^\beta$ possesses its own PBG in the considered wavelength range. Combination of these structures in a complex three-component three-periodic structure can give both broadening of the PBG and essential modification of the inside PBG modes. The qualities utilized for the simulations are as follows. The optical thickness of each layer is denoted by $nd\cos\theta = \lambda_w/4$ (Bragg condition) where λ_w is the reference wavelength in conformity with He–Ne laser (λ_w = 632.8 nm) [48], which determined physical thicknesses of the layers.

In addition, the refractive index is a function of wavelength (λ) [47,49–51]. In what follows we shall investigate PBG based on the calculated compositional-dependent transmittance for both PCs structures. Light passed vertical incident through the air (n=1) with $\theta_{in} = 0$ to the PC and after a propagation inside a photonic crystal, inserted to the substrate layer.

Fig. 3 displays the transmittance spectrum of the [NS]$^\alpha$ [T]^1 [NS]$^\beta$ structure. One can clearly see that the increase in the periods leads to the formation of the gap in the visible light ranges. In comparison with Fig. 3(a), Fig. 3(b) would show a wider PBG. Basically, since the refractive indices and the number of periods determine the position and the width of PBG, the more stacking of PC layers with different refractive indices would induce a broad PBG. Also, it can be observed from Fig. 3(c) that two PBGs would exist when α = 3. However, a transmission peak (TP) is present between them, being unsuitable for the laser eye protection filters. In addition, increasing the number of

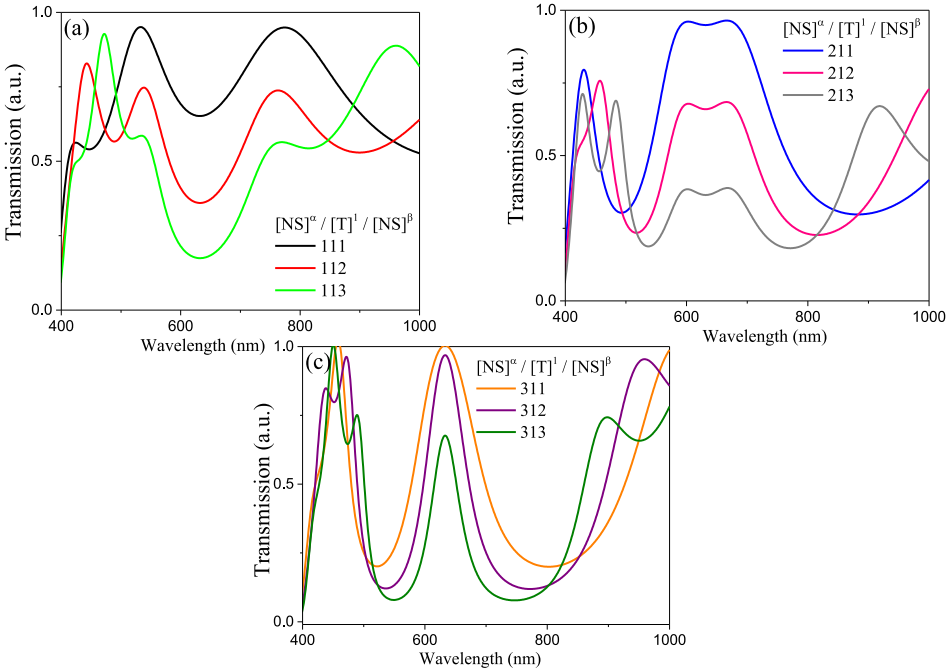

Fig. 3. Transmittance spectra of the $[NS]^{\alpha}$ $[T]^{1}$ $[NS]^{\beta}$ structure calculated for $\beta = 1$, 2 and 3 at: (a) $\alpha = 1$, (b) $\alpha = 2$, and (c) $\alpha = 3$.

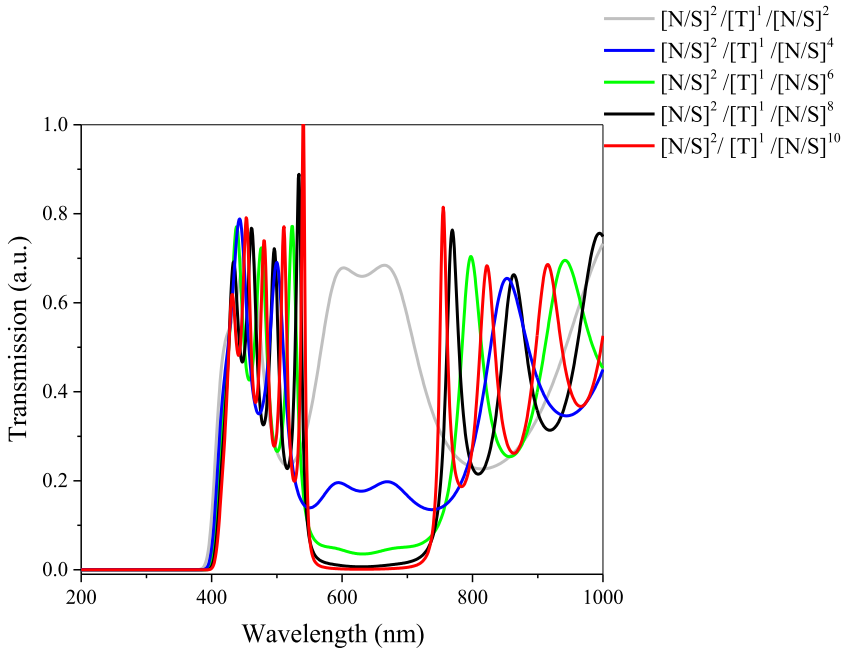

Fig. 4. Transmittance spectrum for the $[NS]^{2}$ $[T]^{1}$ $[NS]^{\beta}$ structure at $\beta = 2$, 4, 6, 8 and 10.

layers in front of the incident wave causes the transmitted wave to be attenuated. Therefore, it is preferred to fix the period α ($\alpha = 2$), while also varying the period β ($\beta = 2$, 4, 6, and 8) in order to achieve a wider PBG in Fig. 4. At $[NS]^{2}$ $[T]^{1}$ $[NS]^{8}$ structure, the PBG with transmittance less than 2% is located in the wavelength range of 571–711 nm, having a width of 140 nm. This is the working range of Krypton laser, Ruby laser, and Diodes laser [48]. A forbidden region with transmittance less than 2% takes place in the ultraviolet region, having a wavelength of less than 400 nm. The above results help us to choose the appropriate number of stacks for PBG. It is also interesting to note that the transmission spectra are similar for both $[NS]^{2}$ $[T]^{1}$ $[NS]^{8}$ and $[NS]^{2}$ $[T]^{1}$ $[NS]^{10}$ structures.

In Fig. 5, $\alpha = 2$ was chosen for the same reason as given for the $[NS]^{2}$ $[T]^{1}$ $[NS]^{8}$ structure. The number of defect layers and position of each layer in the sub-structure β were changed in Fig. 5 and it is evident that as the β increases ($\beta = 2$, 4, 6, and 8), PBG become wider. At $[NS]^{2}[T]^{2}[SN]^{8}$ structure, the PBG is located in the wavelength range (575–705 nm) with a width of 130 nm. For this PBG, the propagation of light is nearly forbidden. It can be seen that the transmission spectra are similar for both $[NS]^{2}$ $[T]^{2}$ $[SN]^{8}$ and $[NS]^{2}$ $[T]^{2}$ $[SN]^{10}$ structures.

Next, we discuss the thickness effect of all layers on the PCs. In Fig. 6, the PBGs slightly shift toward lower wavelengths when decreasing the thickness. In other words, it is also found that increasing the thickness shifts the PBGs toward longer wavelengths. For instance, in the case of the $[NS]^{2}$ $[T]^{1}$ $[NS]^{8}$ structure with $\lambda_{w} = 632.8$ nm,

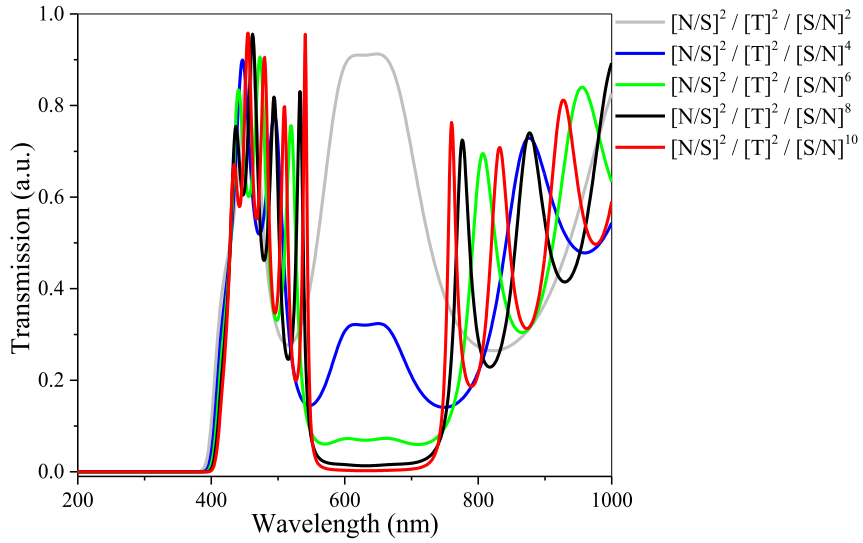

Fig. 5. Transmittance spectrum for the $[NS]^2$ $[T]^2$ $[SN]^{\beta}$ structure at $\beta = 2$, 4, 6, 8 and 10.

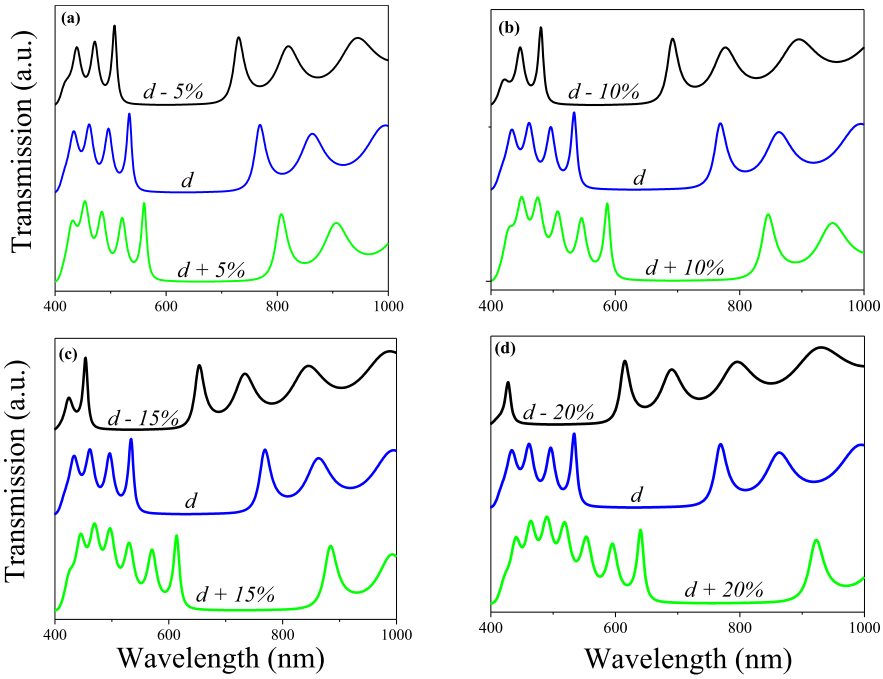

Fig. 6. Simulated transmittance spectrum for the $[NS]^2$ $[T]^1$ $[NS]^8$ structure at different thicknesses.

and $d = \frac{\lambda_w}{4n}$ (d_N = 70.39 nm, d_S = 46.28 nm, d_T = 56.95 nm and $\Lambda = d_N + d_S$ = 116.68 nm), the PBG prevents the propagation of the wave at the corresponding wavelength range of 571–711 nm, having a width of 140 nm (Fig. 6(a)). For $d \pm 5\%$ (being insufficient to change a PBG width), we see that the PBG positions remain almost the same. For λ_w = 569.52 nm and $d - 10\%$ (d_N = 63.35 nm, d_S = 41.65 nm, d_T = 51.26 nm and $\Lambda = d_N + d_S$ = 105.01 nm), the location of the gap gradually blue shifts to the wavelength range of 514–640 nm, having a width of 126 nm. This results in a narrower band gap width, being the working range of the Rhodamine 6G laser and copper vapor laser [48]. In the working range of 514–640 nm, a part of the red, blue, green and yellow lights can be efficiently filtered. For λ_w = 696.08 nm and $d + 10\%$ (d_N = 77.43 nm, d_S = 50.91 nm, d_T = 62.65 nm and $\Lambda = d_N + d_s$ = 128.34 nm), the location of the gap red shifts to the wavelength range of 628–782 nm, having a width of 154 nm. This results in a wider band gap width, being the working range of the Alexandrite laser and Ruby laser [48]. In this region, orange, yellow and red lights can be filtered well. The optical path length changes with changing the layer thickness, giving rise to a shift in the position of the PBG of the whole structure.

For $[NS]^2$ $[T]^2$ $[SN]^8$ structure with λ_w = 632.8 nm, the PBG prohibited the propagation of wave at a corresponding wavelength range (575–705 nm) with a width of 130 nm. For λ_w = 569.52 nm and $d - 10\%$ the location of the gap gradually blue-shifted to wavelength ranges (517–635 nm) with a width of 118 nm. For λ_w = 696.08 nm and $d + 10\%$ the gap location red-shifted to wavelength range (632–776 nm) with a width of 144 nm. (Table 1)

In Fig. 7, we have plotted the relative PBG width versus working wavelength for both structures. One can see that the PBG width increases with increasing the working wavelength and follows the linear fitted equations: $Y = -2.58 + 0.22$ X, and $Y = 0.29 + 0.20$ X. These results help us to choose the appropriate working wavelength for PBG, which may provide further opportunities in the design and optimization of PCs.

Table 1
PBG location and width at different thickness for the $[NS]^2$ $[T]^2$ $[SN]^8$ structure.

Thickness (nm)	PBG location (nm)	PBG width (nm)
d – 5%	[546–670]	124
d + 5%	[603–741]	138
d – 10%	[517–635]	118
d + 10%	[632–776]	144
d – 15%	[489–600]	111
d + 15%	[661–811]	150
d – 20%	[460–564]	104
d + 20%	[690–846]	156

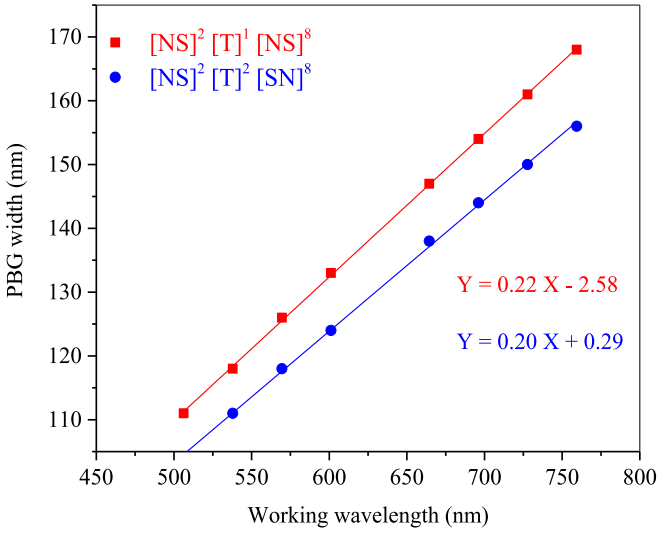

Fig. 7. Relative bandwidth of the PBG as a function of working wavelength.

Fig. 8 shows that the $[NS]^2$ $[T]^1$ $[NS]^8$ structure has a forbidden region under 518 nm, whereas the forbidden band occurs under 515 nm for the $[NS]^2$ $[T]^2$ $[SN]^8$ structure. In other words, when d decreases more than 27%, the band gap will disappear, thus disturbing the performance of the PC due to the fabrication error of more than ± 26%.

Further to clarify how the TiO_2 thickness affects the PCs performance and optimize performance of PCs, the simulated transmittance spectrum of $[NS]^2$ $[T]^1$ $[NS]^8$ structure (Fig. 9) and $[NS]^2$ $[T]^2$ $[SN]^8$ structure (Fig. 11) with different d_{TiO_2}, displayed in Figs. 9–11. Defining the d_{TiO_2} as the ±5% rise from $d = \lambda_w/4n$. At $[NS]^2$ $[T]^1$ $[NS]^8$ structure, and from Fig. 9, it is clear that increasing the thickness of the TiO_2 thin film almost does not change the positions of the PBG and also the PBG width keeps constant, whereas, the width of PBG show a noticeable change with the increasing in TiO_2 thicknesses as ± 10%, as shown in Fig. 10. So, Fabrication error by ± 10% decrease the width of PBG, whereas the PBG width remains steady at ± 5%.

The effect of fabrication error by ± 5% at $[NS]^2$ $[T]^2$ $[SN]^8$ structure specifically investigated in Fig. 11, It is clearly noted that the structure has the PBG with slightly bending edges, the width of PBG decrease and disturb the performance of the PC.

To examine the effect of incident angle on the band gap width, the variation diagrams of band gap from 0° to 60° for both TE and TM modes and for both PCs were obtained by calculations. With the increase of the incident angle from 0° to 60°, the bad gap width became wider. As the result in Fig. 12(a), the gap width was 140 nm at 0°, 171 nm at 30°, and 234 nm at 60°. In Fig. 12(c), the gap width was 130 nm at 0°, 172 nm at 30°, and 239 nm at 60°. This showed that the incident angle affected the PBG width, and the band gap width reached the maximum at TE mode when the incident angle θ was 60°. In Fig. 12(b), the gap width was 147 nm at 30°, and 239 nm at 60°. In Fig. 12(d), the gap width was 142 nm at 30°, 121 nm at 60°.

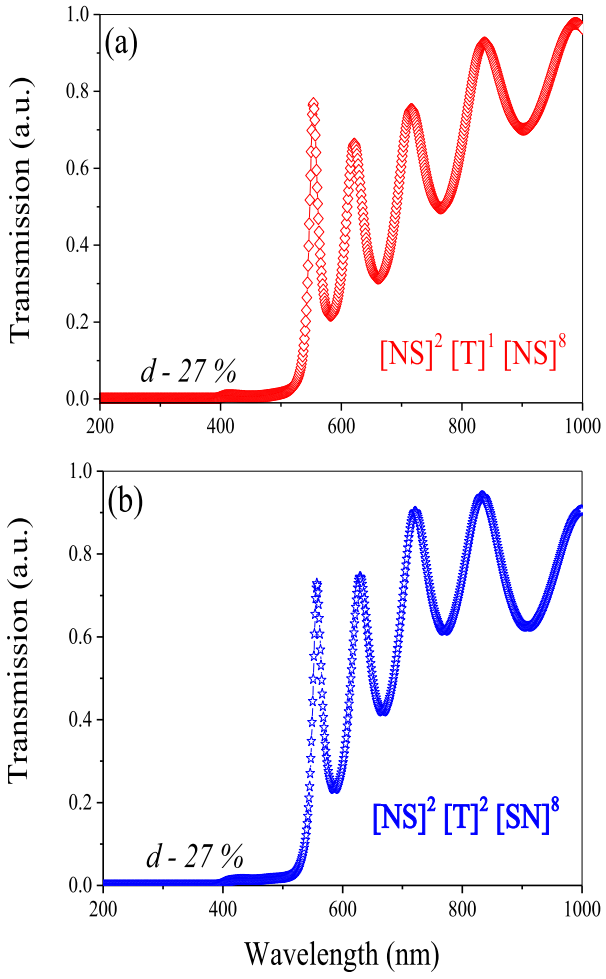

Fig. 8. Simulated transmittance spectrum for both PCs at d - 27%.

In this second part, we will localize and enhance the electric field intensity in a defect layer (TiO_2). We demonstrate that the electric field intensity depends on the number of periods, the thickness of layers, and the angle of incident. We assume that λ_w = 632.8 nm, θ = 0 and $d = \frac{\lambda_w}{4n}$. The index of refraction of the layer is n_N = 2.3, n_S = 3.8 and n_T = 2.6. The variation of the electric field intensity showed in Fig. 13 indicates that the intensity increases in the TiO_2, arising from the strong resonant scattering and interference effects. Furthermore the electric field intensity decreased in the bottom sub-structure with low oscillations, so second sub-structure acted as a Bragg mirror to reflect the light back, which caused the electric field decayed on these layers. Furthermore, the optimal configuration is $[NS]^2$ $[T]^2$ $[SN]^8$ structure corresponding to strong localization of light in defect layer. This permits a strong interaction between light and matter, which is important for enhancement of function of semiconductor photocatalyst.

To study the impact of the number of periods we present the maximum electric field intensity for various number of period α and β, with other parameters being the same as in Fig. 13, with α = 1 and with varied β the maximum electric field intensity it is too weak and gradually tended to be stable in both structures. It should be noted that the colors represent the maximum electric field intensity. In the case of α = 2 and vary β, the maximum electric field intensity increases as β increases; while, the effect of β on the maximum electric field intensity is very inconsiderable after a certain number, β = 5, in the $[NS]^{\alpha}$ $[T]^1$ $[NS]^{\beta}$ structure and β = 6 in $[NS]^{\alpha}$ $[T]^2$ $[SN]^{\beta}$ structure. (Fig. 14)

The transmittance under various optical thickness of defect-layer for both structures is depicted in Fig. 15. Defect layer thicknesses are

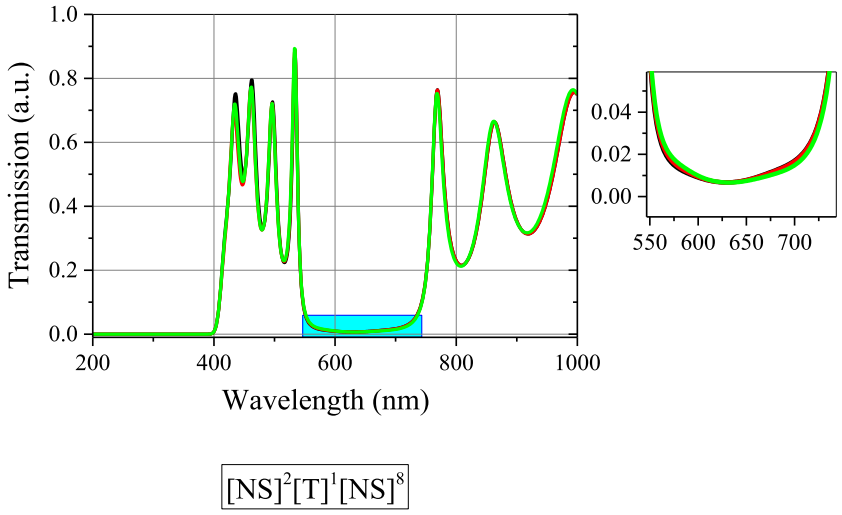

Fig. 9. Simulated transmittance spectrum for the $[NS]^2$ $[T]^1$ $[NS]^8$ structure at $d_{TiO2} \pm 5\%$.

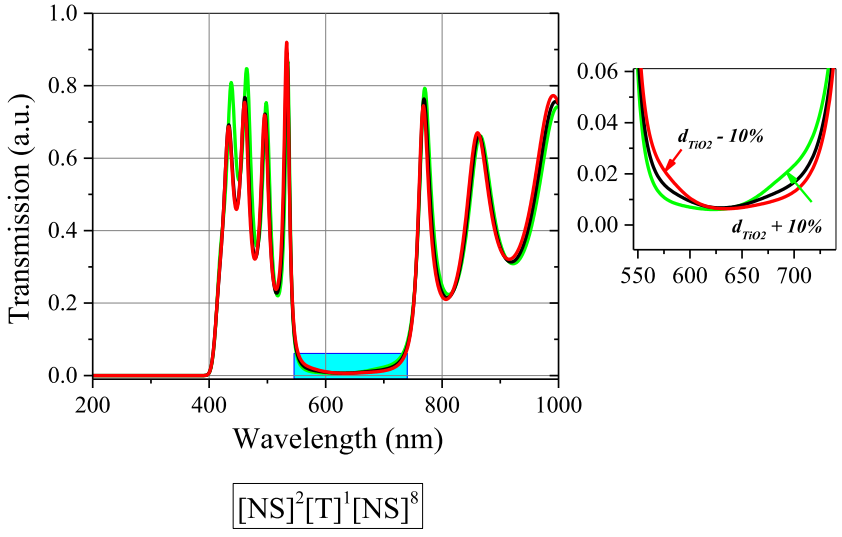

Fig. 10. Simulated transmittance spectrum for the $[NS]^2$ $[T]^1$ $[NS]^8$ structure at $d_{TiO2} \pm 10\%$.

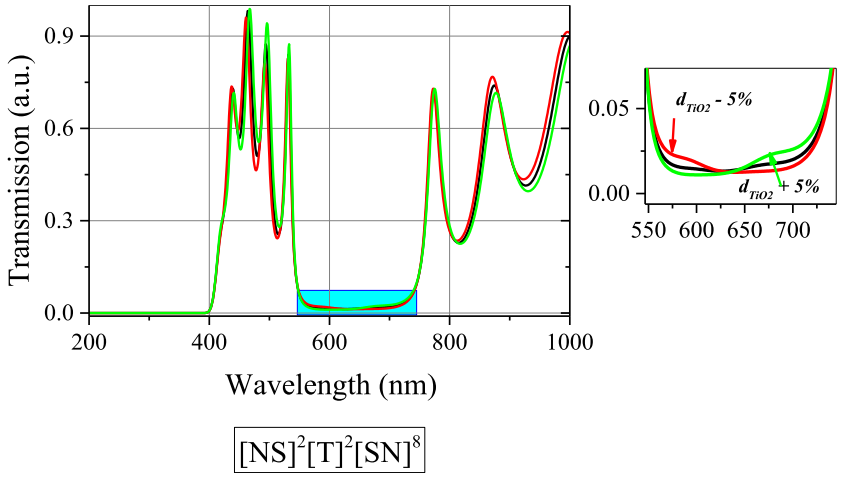

Fig. 11. Simulated transmittance spectrum for the $[NS]^2$ $[T]^2$ $[SN]^8$ structure at $d_{TiO2} \pm 5\%$.

$d = \frac{\lambda_w}{4n}, \frac{\lambda_w}{2n}, \frac{3\lambda_w}{4n}, \frac{\lambda_w}{n}$. It is interesting to see that the light harvesting of TiO_2 in the $[NS]^2$ $[T]^1$ $[NS]^8$ structure disappears when d is an even number of the first thickness (i.e., $d = \frac{\lambda_w}{2n}, \frac{\lambda_w}{n}, \ldots$). This is because more destructive interference is involved in the interior of the

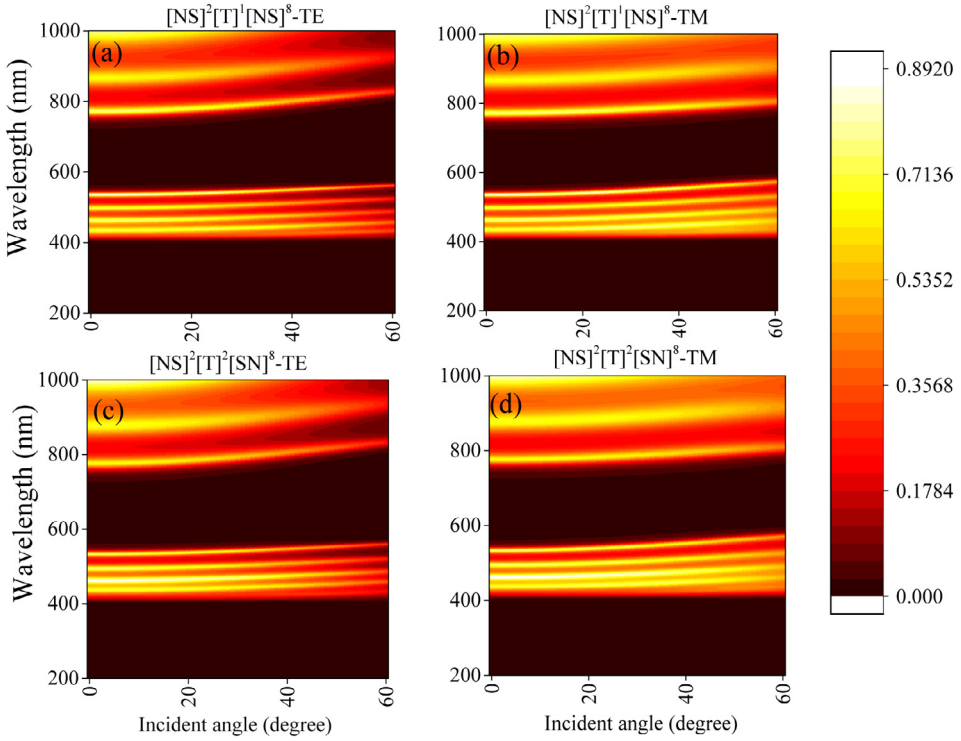

Fig. 12. Transmissivity spectra of TE- and TM-modes versus wavelength and incident angle θ for both PCs.

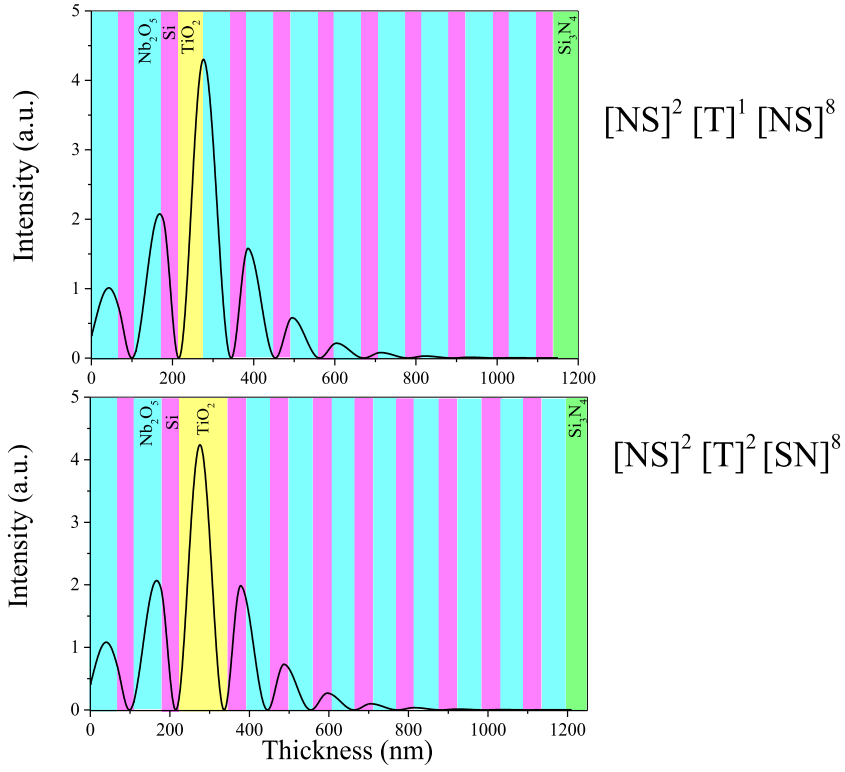

Fig. 13. Variation of the electric field intensity, versus the thickness.

structure, and localize at TiO_2 layer when d is an odd number of the first thickness, (i.e., $d = \frac{\lambda_w}{4n}, \frac{3\lambda_w}{4n}, \ldots$). Moreover in $[NS]^2\ [T]^2\ [SN]^8$ structure the number of the envelop oscillations increases by increasing the defect-layer optical thickness.

To investigate the angle dependent optical properties of PCs and discuss its possibility of desired photocatalytic photonic crystal, the simulated electric field intensity under different incident angles have been calculated and shown in Fig. 16. It can be clearly seen that,

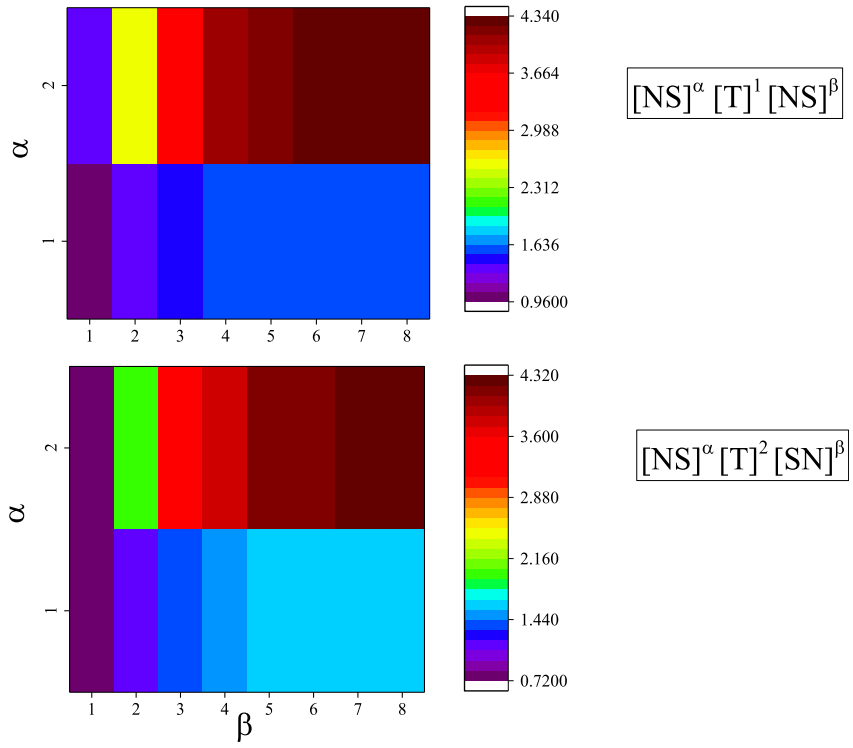

Fig. 14. The maximum electric field intensity versus the number of periods.

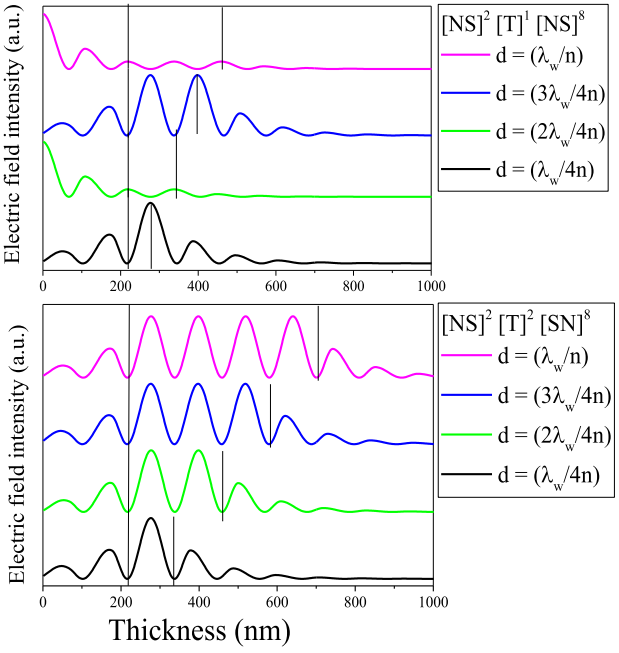

Fig. 15. Electric field intensity versus the various defect-layer thickness $d = \frac{\lambda_{wc}}{4n}, \frac{\lambda_{wc}}{2n}, \frac{3\lambda_{wc}}{4n}, \frac{\lambda_{wc}}{n}$ for both structures.

compared to the TM modes, at TE modes the electric field intensity significantly decreased as the incident angle increased. Also, it can be seen that the $[NS]^2$ $[T]^1$ $[NS]^8$ structure-TE has an intensity equal to 4.3 and $[NS]^2$ $[T]^1$ $[NS]^8$ structure-TE has an intensity equal to 4.2 under normal light, which decreased to 2.29 in TE mode for both structures and 1.44 for $[NS]^2$ $[T]^1$ $[NS]^8$-TM structure and 1.33 in $[NS]^2$ $[T]^1$ $[NS]^8$-TM structure , when the incident angle θ was 60 degree, so best enhancement effect can be achieved under the normal incident light.

4. Conclusion

A new design of the one-dimensional three-periodic photonic crystal was proposed, and the influence of different parameters on the photonic band gap and electric field distribution was analyzed. The theoretical calculations based on transfer matrix method were carried out using MATLAB software. Two various structures based on the layer order and the number of periods were introduced as {A$[NS]^{\alpha}$ $[T]^1$ $[NS]^{\beta}$ Sub} and {A$[NS]^{\alpha}$ $[T]^2$ $[SN]^{\beta}$ Sub}. When the number of periods was $[NS]^2$ $[T]^1$ $[NS]^8$ and $[NS]^2$ $[T]^2$ $[SN]^8$, two PBGs were located in the ultraviolet and the visible regions. For strong localization of light in the defect layer, the optimal configuration was found to be $[NS]^2$ $[T]^2$ $[SN]^8$ structure. The PBG red-shifted and the gap width increased with increasing the layer thickness, whereas, the location of the gap gradually blue-shifted and the gap width became narrower when decreasing the layer thickness. When the defect layer thickness increased, the PBG width decreased in both structures, but having different quantities. For $[NS]^2$ $[T]^1$ $[NS]^8$ structure, the light harvesting in the TiO_2 layer disappeared when d was even number of the first thickness, and localize at TiO_2 layer when d was an odd number of the first thickness. Moreover for $[NS]^2$ $[T]^2$ $[SN]^8$ structure, the number of the envelop oscillations increased by increasing the defect-layer optical thickness. The incident angle affected the PBG width, and the band gap width reached the maximum at the TE mode when the incident angle θ was 60°. The electric field intensity significantly decreased as the incident angle increased.

Declaration of competing interest

The authors declare that they have no known competing financial interests or personal relationships that could have appeared to influence the work reported in this paper.

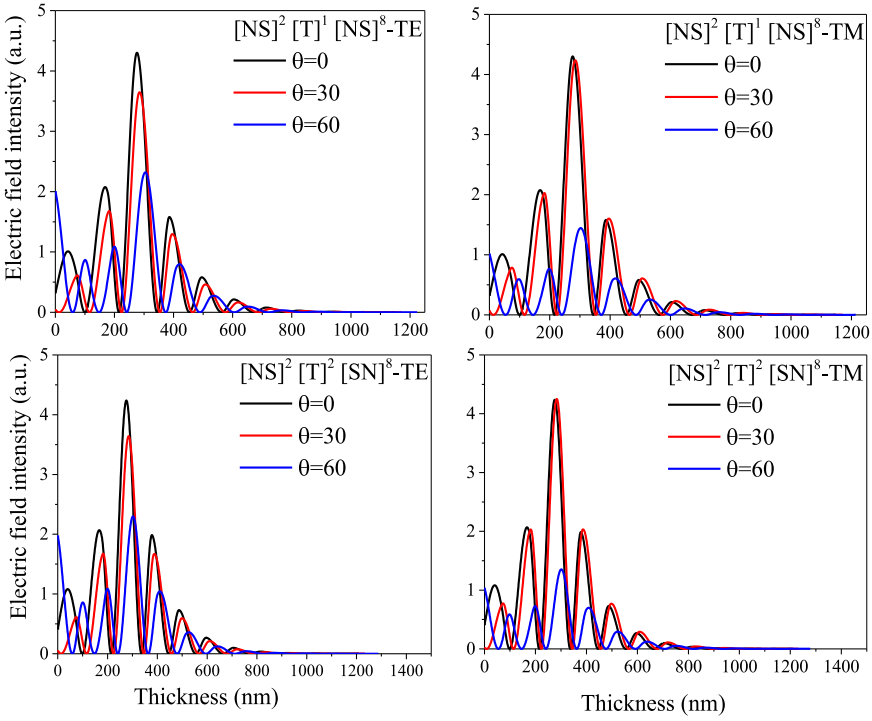

Fig. 16. Electric field intensity versus the thickness for incident angles of 0, 30 and 60 degrees.

References

[1] Y. Li, R. Li, H. Bian, H. Hu, K. Zhang, P. Han, Opt. Commun. 474 (2020) 126110, http://dx.doi.org/10.1016/j.optcom.2020.126110.

[2] M. Moradi, H. Alisafaee, M. Ghanaatshoar, Physica B 405 (2010) 4488–4491, http://dx.doi.org/10.1016/j.physb.2010.08.020.

[3] M. Moradi, M. Ghanaatshoar, Opt. Commun. 283 (2010) 5053–5057, http://dx.doi.org/10.1016/j.optcom.2010.07.039.

[4] G. Collins, E. Armstrong, D. McNulty, S. O'Hanlon, H. Geaney, C. O'Dwyer, Sci. Technol. Adv. Mater. 17 (2016) 563, http://dx.doi.org/10.1080/14686996.2016.1226121.

[5] E. Yablonovitch, Phys. Rev. Lett. 58 (1987) 2059–2062, http://dx.doi.org/10.1103/physrevlett.58.2059.

[6] J.D. Joannopoulos, S.G. Johnson, J.N. Winn, R.D. Meade, Photonic Crystals: Molding the Flow of Light, Princeton University Press, 2011.

[7] J.D. Joannopoulos, P.R. Villeneuve, S. Fan, Nature 386 (1997) 143, http://dx.doi.org/10.1038/386143a0.

[8] Q. Gong, X. Hu, Photonic Crystals: Principles and Applications, Pan Stanford, 2014.

[9] D.W. Prather, A. Sharkawy, S. Shi, J. Murakowski, G. Schneider, Photonic Crystals: Theory, Applications and Fabrication, John Wiley & Sons, 2009.

[10] J.M. Louritioz, H. Benisty, V. Berger, J.M. Gerard, D. Maystre, A. Tchelnokov, Photonic Crystals: Towards Nanoscale Photonic Devices, Springer, Berlin, Heidelber, 2005.

[11] B.K. Singh, S. Tiwari, M.K. Chaudhari, P.C. Pandey, Optik 127 (2016) 6452–6462, http://dx.doi.org/10.1016/j.ijleo.2016.04.067.

[12] X. Xiao, W. Wenjun, L. Shuhong, Z. Wanquan, Z. Dong, D. Qianqian, G. Xuexi, Z. Bingyuan, Optik 127 (2016) 135–138, http://dx.doi.org/10.1016/j.ijleo.2015.10.005.

[13] C. Yue, W. Tan, J. Liu, Superlattices Microstruct. 117 (2018) 252–259, http://dx.doi.org/10.1016/j.spmi.2018.03.023.

[14] N. Ansari, S. Mohammadi, E. Mohebbi, J. Appl. Phys. 127 (2020) 1–7, http://dx.doi.org/10.1063/1.5130149.

[15] N.N. Dadoenkova, Y.S. Dadoenkova, I.S. Panyaev, D.G. Sannikov, I.L. Lyubchanskii, J. Appl. Phys. 123 (2018) 1–8, http://dx.doi.org/10.1063/1.5011637.

[16] C.J. Wu, Z.H. Wang, Prog. Electromagn. Res. 103 (2010) 169–184, http://dx.doi.org/10.2528/PIER10031706.

[17] A. Soman, A. Antony, Sol. Energy 162 (2018) 525–532, http://dx.doi.org/10.1016/j.solener.2018.01.061.

[18] A. Bruyant, G. Lérondel, P.J. Reece, M. Gal, Appl. Phys. Lett. 82 (2003) 3227, http://dx.doi.org/10.1063/1.1574403.

[19] D. Yang, X. Chen, X. Zhang, Opt. Eng. 57 (2018) 1–6, http://dx.doi.org/10.1117/1.OE.57.10.107103.

[20] S. Kim, S. Kurihara, Crystals 9 (2019) 610, http://dx.doi.org/10.3390/cryst9120610.

[21] S.Y. Vetrov, A.Y. Avdeeva, I.V. Timofeev, J. Exp. Theor. Phys. 113 (2011) 755–761, http://dx.doi.org/10.1134/S1063776111140093.

[22] H. Li, W. Jiajun, M. Yating, C. Jiao, C. Xiang'ai, S. Lei, J. Tian, Nanophotonics 9 (2020) 4337–4345, http://dx.doi.org/10.1515/nanoph-2020-0294.

[23] J. Zaghdoudi, M. Kanzari, Optik 160 (2018) 189–196, http://dx.doi.org/10.1016/j.ijleo.2018.01.129.

[24] F.K. Mbakop, N. Djongyang, D.Raïdandi, J. Eur. Opt. Soc.-Rapid Publ. 12 (2016) 23, http://dx.doi.org/10.1186/s41476-016-0026-4.

[25] R. Dalmis, O.Y. Keskin, N.F. AkAzem, I. Birlik, Ceram. Int. 45 (2019) 21333–21340, http://dx.doi.org/10.1016/j.ceramint.2019.07.119.

[26] C. Ming, L. Chunfei, X. Mai, W. Weibiao, M. Shaojie, X. Yuxue, Opt. Laser Technol. 39 (2007) 214–218, http://dx.doi.org/10.1016/j.optlastec.2005.02.005.

[27] A. Douplik, G. Saiko, I. Schelkanova, V.V. Tuchin, Lasers for Medical Applications, Woodhead Publishing, 2013, pp. 47–109, http://dx.doi.org/10.1533/9780857097545.1.47.

[28] W. Yuan, L. Ping, C. Sheng-Li, W. Ai-Jun, Catal. Surv. Asia 23 (2019) 23–32, http://dx.doi.org/10.1007/s10563-018-9259-0.

[29] Q. Guo, C. Zhou, Z. Ma, X. Yang, Adv. Mater. 50 (2019) 190197, http://dx.doi.org/10.1002/adma.201901997.

[30] J. Schneider, M. Matsuoka, M. Takeuchi, J. Zhang, Y. Horiuchi, M. Anpo, D.W. Bahnemann, Chem. Rev. 114 (2014) 9919–9986, http://dx.doi.org/10.1021/cr5001892.

[31] B. Esmaeilzadeh, M. Moradi, F. Jahantigh, J. Magn. Magn. Mater. 460 (2018) 207–212, http://dx.doi.org/10.1016/j.jmmm.2018.04.003.

[32] W. Zhang, Q. Wang, C. Zhao, Y. Song, Opt. Commun. 437 (2019) 44–49, http://dx.doi.org/10.1016/j.optcom.2018.12.033.

[33] M. Moradi, M. Ghanaatshoar, Modern Phys. Lett. B 30 (2016) 1–8, http://dx.doi.org/10.1142/S0217984915502589.

[34] F. Zhang, R. Jin, J. Chen, C. Shao, W. Gao, L. Li, N. Guan, J. Catal. 232 (2005) 424–431, http://dx.doi.org/10.1016/j.jcat.2005.04.014.

[35] J. Yang, D. Wang, H. Han, C. Li, Acc. Chem. Res. 46 (2013) 1900–1909, http://dx.doi.org/10.1021/ar300227e.

[36] Esmailzadeh Behnam, Moradi Mehrdad, Enhancement of Kerr Signal in Co Thin Films Incorporating Ag Nanoparticles Surrounded by TiO_2, J. Superconduct. Novel Magnet. 31 (5) (2018) 1483–1488, http://dx.doi.org/10.1007/s10948-017-4345-5.

[37] M. Fan, S. Hu, B. Ren, J. Wang, Powder Technol. 235 (2013) 27–32, http://dx.doi.org/10.1016/j.powtec.2012.09.042.

[38] J. Yan, G. Wu, N. Guan, L. Li, Appl. Catal. B 152–153 (2014) 280–288, http://dx.doi.org/10.1016/j.apcatb.2014.01.049.

[39] X. Xiao, G. Dong, C. Xu, H. He, H. Qi, Z. Fan, J. Shao, Appl. Surf. Sci. 255 (2008) 2192–2195, http://dx.doi.org/10.1016/j.apsusc.2008.07.071.

[40] G. Agarwal, G.B. Reddy, J. Mater. Sci. Mater. Electron. 16 (2005) 21–24, http://dx.doi.org/10.1007/s10854-005-4953-x.

[41] W.J. Chen, X. Sun, Y. Liu, M. Huang, W. Xu, X. Pan, Q. Wu, Z. Yi, ACS Appl. Nano Mater. 3 (2020) 2573–2581, http://dx.doi.org/10.1021/acsanm.9b02621.
[42] J.M. Luque-Raigon, J. Halme, H. Miguez, J. Quant. Spectrosc. Radiat. Transfer 134 (2014) 9–20, http://dx.doi.org/10.1016/j.jqsrt.2013.10.007.
[43] P. Yeh, A. Yariv, Optical waves in crystals: Propagation and control of laser radiation, in: Wiley Series in Pure and Applied Optics, 589, 1984.
[44] E. Xifre Perez, Design, Fabrication and Characterization of Porous Silicon Multilayer Optical Devices, Universitat Rovira i Virgili, Escola Tècnica Superior d Enginyeria, 2007.
[45] C.C. Katsidis, D.I. Siapkas, Appl Opt. 41 (2002) 3978–3987, http://dx.doi.org/10.1364/AO.41.003978.
[46] N. Ben Ali, V. Dhasarathan, H. Alsaif, Y. Trabelsi, Physica B 582 (2020) 411918, http://dx.doi.org/10.1016/j.physb.2019.411918.
[47] D.E. Aspnes, A.A. Studna, Phys. Rev. 27 (1983) 985–1009, http://dx.doi.org/10.1103/PhysRevB.27.985.
[48] M.J. Weber, Handbook of Laser Wavelengths, CRC Press, 1999.
[49] J.R. Devore, J. Opt. Soc. Amer. 41 (1951) 416–419, http://dx.doi.org/10.1063/1.365938.
[50] K. Luke, Y. Okawachi, M.R.E. Lamont, A.L. Gaeta, M. Lipson, Opt. Lett. 40 (2015) 4823–4826, http://dx.doi.org/10.1364/CLEO_SI.2015.STu4I.8.
[51] K.N. Chen, C.M. Hsu, J. Liu, Y.C. Liou, C.F. Yang, Investigation of Antireflection Nb_2O_5 Thin Films by the Sputtering Method under Different Deposition Parameters, Micromachines 7 (2016) 151, http://dx.doi.org/10.3390/mi7090151.